Direct observation of competition between charge order and itinerant ferromagnetism in the van der Waals crystal $Fe_{5-x}GeTe_2$

Xuchuan Wu,[*] Le Lei,[*] Qiangwei Yin,[*] Ning-Ning Zhao,[*] Man Li, Zilu Wang, Qingxin Liu, Wenhua Song, Huan Ma, Pengfei Ding, Zhihai Cheng,[†] Kai Liu,[‡] Hechang Lei,[§] and Shancai Wang[‖]

Department of Physics, Beijing Key Laboratory of Optoelectronic Functional Materials & Micro-nano Devices, Renmin University of China, Beijing 100872, China

(Received 1 June 2021; revised 29 July 2021; accepted 10 September 2021; published 1 October 2021)

The interplay of symmetry-breaking ordered states, such as superconductivity, charge density waves, magnetism, and pseudogaps, is a fundamental issue in correlated systems. Periodic modulation and antiferromagnetism often coexist in the proximity of phase diagram region in high-T_c superconductors. It is also worth noting that different order states appear in a situation on comparable temperature scales, so these orders are intertwined and competing on the same footing. The magnetism of vdW material $Fe_{5-x}GeTe_2$, with one of the highest reported bulk Curie temperatures, is found to be sensitive to thermal history and external magnetic field. However, the temperature-dependent magnetization with two characteristic points still lacks a unified picture to describe it. Using angle-resolved photoemission spectroscopy, scanning tunneling microscopy, magnetic property measurements, and first-principles calculations, the complex yet intriguing magnetic behaviors are gradually unveiled. A competition mechanism between charge order and ferromagnetism is proposed and firmly observed by experimental measurements. As the ferromagnetic order strengthens at low temperature, the charge order will be suppressed. Exchange splitting in itinerant ferromagnetism plays a significant role in the temperature evolution of band structure and causes a Lifshitz transition, which provides more control means to realize novel devices at room temperature.

DOI: 10.1103/PhysRevB.104.165101

I. INTRODUCTION

Charge order displayed as a periodic modulation in real space is believed to be intimately connected to the correlated electronic phases, such as high-T_c superconductivity in cuprates [1–3] and pnictides [4,5], and rotational symmetry breaking of the moiré superstructure in the recently studied magic-angle twisted bilayer graphene [6]. Two-dimensional van der Waals (vdW) crystals with intrinsic magnetism have great potential for application in spintronic devices and challenges in physics. To date, the demand for versatile performance improvement and efficient information storage in postsilicon electronics has to be settled, and it sparked extensive research in the two-dimensional vdW magnetic materials by combining complementary properties in vdW heterostructures [7].

Intrinsic magnetic vdW materials such as chromium trihalides, CrX_3 (X = Cl, Br, I), and the ternary compound Fe_nGeTe_2 have garnered significant attention because of their intriguing magnetic properties [8–16]. The ferromagnetic cleavable vdW metal $Fe_{3-x}GeTe_2$ has high Curie temperature $T_c = 230$ K. More importantly, a room-temperature $T_c = 270 \sim 300$ K magnet in the Fe-Ge-Te compound $Fe_{5-x}GeTe_2$ has been synthesized [17–24]. The cobalt-doped $(Fe_{1-x}Co_x)_5GeTe_2$ has an even higher Curie temperature T_c and stronger magnetic anisotropy and antiferromagnetic state [20,23], which provide an efficient way to manipulate spintronic devices [25–27]. A wide scope of correlation phenomena in 2D materials is also observed, including charge density waves [28–32], superconductivity [33–36], and Mott insulators [37–39]. They are driven by factors such as electron correlations, electron-phonon coupling, or electronic band topology [9].

It is reported that a superstructure modulation vector $\boldsymbol{q} = (1/3, 1/3, 1)$ was detected by the selected-area electron diffraction above $T = 100$ K in $Fe_{5-x}GeTe_2$ and faded below 100 K [18]. A $\sqrt{3}a \times \sqrt{3}a\, R30^\circ$ short-range order reflected by the fast Fourier transform (FFT) pattern of the high-angle annular dark field (HAADF) image along $[1\bar{1}0]$ was revealed [21]. The drop of the resistivity curve, ordinary Hall coefficient sign change, and the behavior of the Seebeck coefficient around 110 K [17,18] in $Fe_{5-x}GeTe_2$ indicate an obvious evolution of electronic band structure and possible change of Fermi surface topologies. However, the influence of the order on the electronic structure in ferromagnet $Fe_{5-x}GeTe_2$ has yet to be revealed by clear spectroscopy. A complementary mechanism is still not put forward to explain the complexity of the magnetization curve especially the formation of the order parameter below approximately 165 K. These phenomena are intriguing to inspect by more spectroscopic probes.

[*]These authors contributed equally to this work.
[†]zhihaicheng@ruc.edu.cn
[‡]kliu@ruc.edu.cn
[§]hlei@ruc.edu.cn
[‖]SCW@ruc.edu.cn

In this work, by combining angle-resolved photoemission spectroscopy (ARPES), magnetization measurements, scanning tunneling microscopy (STM), and first-principles calculations, we confirm the existence of a $\sqrt{3}a \times \sqrt{3}a\ R30^\circ$ periodic modulation and carefully explore its impact on the electronic structure. We speculate on a competitive mechanism between the ferromagnetism and the charge order in $Fe_{5-x}GeTe_2$, which could lead to an electronic symmetry breaking and drive the magnetic transitions. Exchange splitting in an itinerant ferromagnetic model could qualitatively explain the spin-polarized band shifting and the Lifshitz transition, which leads to the carriers change from hole dominance to electron reported in transport measurements [17,18]. The periodic modulation $\sqrt{3}a \times \sqrt{3}a\ R30^\circ$ observed by STM and corresponding features in ARPES measurement at two characteristic temperature points can be interpreted by the temperature-dependent competitive mechanism well.

II. RESULTS

Figure 1(a) shows a schematic of the average crystal structure determined by a single-crystal x-ray diffraction (XRD) pattern. The Fe-Ge sublayers stack along the c direction in the centrosymmetric space group $R\bar{3}m$ (No. 166) with $a = 4.0375(5)$ and $c = 29.191(1)$ by Rietveld refinement. The cleavage plane oriented along the c axis is marked by the red arrow, due to the adjacent Te layers connected by weak vdW interaction. The vacancy of Fe and the tendency to form atomic short-range order/disorder lead to an uncertain x in $Fe_{5-x}GeTe_2$ [21]. The Fe vacancies are identified as $Fe_{4.78(4)}GeTe_{2.13(1)}$, when setting the content of Ge as 1 derived from the XRD pattern and the energy-dispersive x-ray (EDX) spectrum. The Fe(1) and Ge are split sites, where Fe(1) can be above or below the neighboring Ge, or can be vacant.

The magnetization $M(T)$ for $B = 0.01$ T, 0.1 T, and 1 T along the ab plane are shown in Fig. 1(e). The magnetization curves clearly exhibit the FM transition at approximately 300 K. It shows two clear transitions at $T_{c2} \approx 165$ K ($B = 0.01$ T at $T_{c2} \approx 180$ K) and $T_{c1} \approx 110$ K successively below Curie temperature, marked by the black arrows. When cooling below T_{c2} at low field $B = 0.01$ T or $B = 0.1$ T, the $M(T)$ curves start to decline, but the one at $B = 1$ T rises. An order parameter is formed at T_{c2} and competes with the magnetism, and it can be suppressed under a relatively large magnetic field at $B = 1$ T.

To specify the formation of the order, the STM measurement was performed on the cleavage plane in $Fe_{5-x}GeTe_2$. Figure 1(b) shows the atomic-resolution STM image of the $Fe_{5-x}GeTe_2$ cleavage plane. The atomic-resolution STM image represents the Te atoms on the surface of the $Fe_{5-x}GeTe_2$ cleavage plane. The line profile shows the in-plane lattice constant of ~0.41 nm, which is consistent with the reported results of the STEM and XRD measurements [18,21]. The spatial distribution of the electronic states is studied by the dI/dV conductance map. The dI/dV conductance map shown in Fig. 1(c) clearly verified the trimerization of electronic states indicated by the white triangles. The FFT image [Fig. 1(d)] of the dI/dV conductance map can distinguish the $\sqrt{3}a \times \sqrt{3}a\ R30^\circ$ periodic modulation induced by the charge order and the primitive 1×1 structure simultaneously.

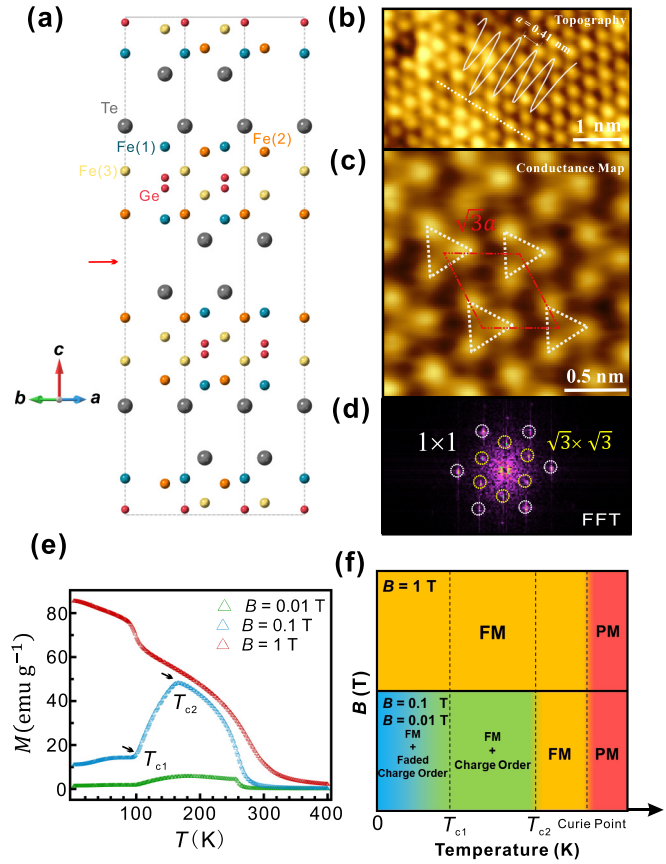

FIG. 1. (a) Schematic of $Fe_{5-x}GeTe_2$ crystal structure with Fe-Ge-Te slab stacked along c axis, where Fe(1) and Ge are split sites that allow for local atomic order and disorder. (b) Atomic-resolution topography STM image ($V_b = -10$ mV, $I_t = -100$ pA) of $Fe_{5-x}GeTe_2$ cleavage plane indicated by the red arrow in (a). Line profile along the white dashed line indicates the Te-Te interval 0.41 nm. (c) The dI/dV conductance map ($V_b = -50$ mV, $I_t = -100$ pA) of $Fe_{5-x}GeTe_2$. (d) The corresponding fast Fourier transform (FFT) image of (c), where the white and yellow dotted circles in the FFT image indicate the 1×1 and $\sqrt{3}a \times \sqrt{3}a\ R30^\circ$ structures, respectively. (e) Temperature-dependent magnetization curves for $H \parallel ab$ at different field indicated by the colors. (f) Temperature-dependent phase diagram of $Fe_{5-x}GeTe_2$ crystal in different magnetic fields.

To explore the influence of the charge order on electronic structures, Fig. 2 shows the ARPES measurement and DFT calculations of $Fe_{5-x}GeTe_2$ in the magnetic state at low temperature $T = 30$ K. As shown in Figs. 2(a) and 2(b), the Fermi surface (FS) contour at low temperature $T = 30$ K consists of a circular (α) and a hexagonal (β) hole pocket centered at the Γ point, a nearly triangular electron pocket (γ) around at the K point, and a small electron pocket (δ) at the M point. The DFT-calculated FS with magnetization in the c plane and chemical component at $x = 0.33$ ($Fe_{4.67}GeTe_2$) (see the methods for the DFT details in the Supplemental Material [40]) is consistent with the experimental crystal $x = 0.22$ ($Fe_{4.78}GeTe_2$) determined by EDX. Despite the matrix element effect, the FS topology conforms more with the C_6 rotational symmetry at low temperature, which meets the expectation from the calculated FS [Fig. 2(b)].

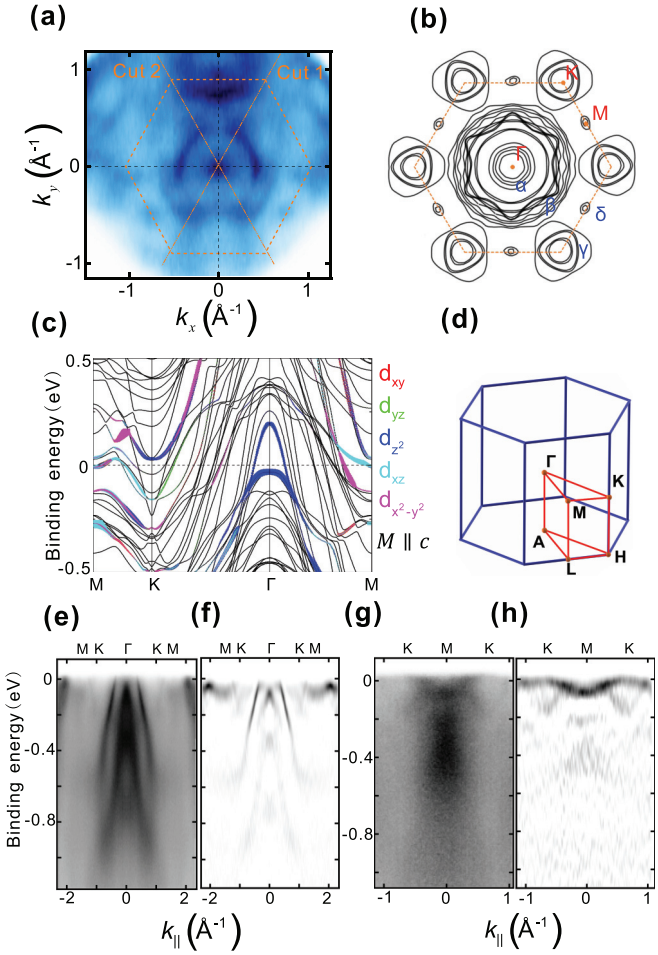

FIG. 2. ARPES band mapping at 30 K and DFT band calculations for $Fe_{5-x}GeTe_2$. (a) Photoemission intensity map at the E_F in k_x-k_y plane at 30 K, and the orange hexagon indicates the Brillouin zone (BZ) boundary. The ARPS spectra taken on a nearly stoichiometric single crystal of $Fe_{5-x}GeTe_2$ ($x = 0.22$). (b) The calculated FSs at $k_z = 0$ plane and the high-symmetry points are presented in (d). (c) The calculated band structures along the high-symmetry lines, and the magnetic moments are given by $M \parallel c$. The calculated Fe $3d$ orbital contributions is imposed on (c). (d) The BZ of $Fe_{5-x}GeTe_2$ with the high-symmetry points and lines indicated. (e)–(f) and (g)–(h): The photoemission intensity and their second derivative of the intensity plots along the Γ-K-M direction and the K-M-K direction, respectively.

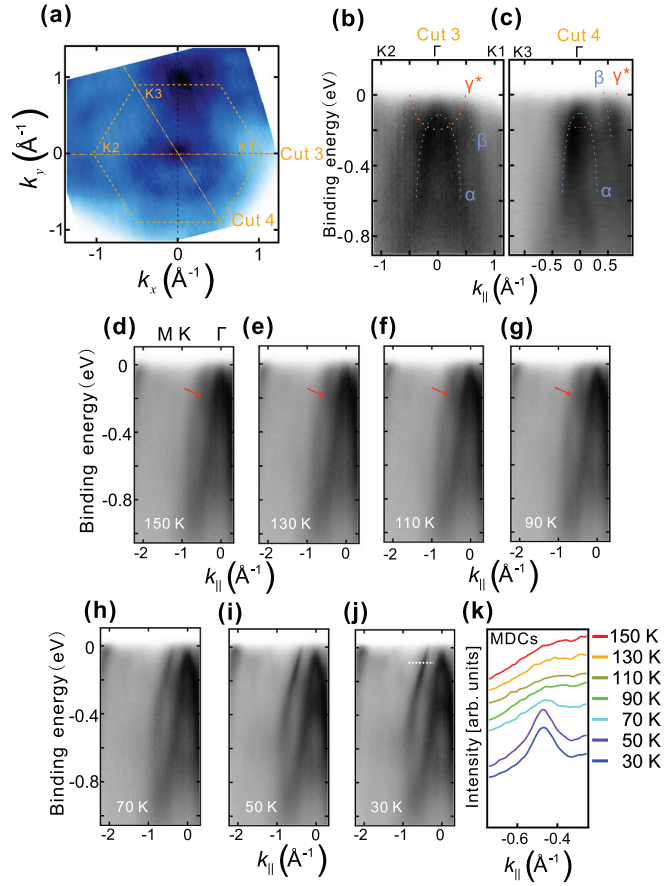

FIG. 3. Temperature dependence of the band structure. (a) Photoemission intensity map at E_F in k_x-k_y plane at 150 K. (b)–(c): The intensity maps along the cut 3 and cut 4 indicated in (a), and the shallow electron-like band feature originated from the charge order is labeled γ^*. (d)–(j): Temperature dependence of the band structure along the Γ-K-M direction from $T = 150$ K to 30 K. The electron-like band γ^* is indicated by the red arrows. (k) Temperature-dependent MDCs extracted from (d)–(j) at the binding energy −0.1 eV, indicated by the dashed line in (j).

We have further verified the consistency between the experimental ARPES results [Figs. 2(e)–2(h)] and the calculated band structure [Fig. 2(c)] along the high-symmetry lines with the magnetization along the c axis. In addition, the DFT calculation with magnetization in the ab plane is also performed (see Fig. s3 in the Supplemental Material [40]). Both show the major hole bands (α, β) and electron bands (γ at K, δ at M). A careful comparison between the DFT calculations and the ARPES intensity maps (the second derivative) along the high-symmetry lines also reveals that the DFT calculations ($Fe_{4.67}GeTe_2$) with magnetization along the c axis agree well with the experimental results at low temperature $T = 30$ K. From the photoemission intensity plot along Γ-K-M [Figs. 2(e)–2(f)], there are only hole-like bands around the Γ point and electron-like pockets around the M/K point near the Fermi level, respectively. It is noteworthy that the electron-like band δ is located at 100 meV below E_F and shows a relatively large effective electron mass, which can induce relatively high density of states and influence the Hall conductance.

To understand the behavior of temperature-dependent magnetization, we explore the temperature evolution of the band structure and show this in Fig. 3. At the temperature slightly below T_{c2}, the FS contour displays a prominent C_3 rotational symmetry centered at Γ. The rotational symmetry of the FS is broken from the primitive lattice C_6 to C_3 due to the $\sqrt{3}a \times \sqrt{3}a$ $R30°$ periodic modulation induced by charge order (see Fig. s2 in the Supplemental Material [40] for details). The photoemission intensity plots along the two high-symmetry lines of adjacent $\frac{\pi}{3}$, cut 3 [Fig. 3(b)] and cut 4 [Fig. 3(c)], confirm that the morphology of the hole-like pockets β are distorted compared with the experimental and calculated FS at the low temperature $T = 30$ K (see Fig. s4 in the Supplemental Material [40] for details).

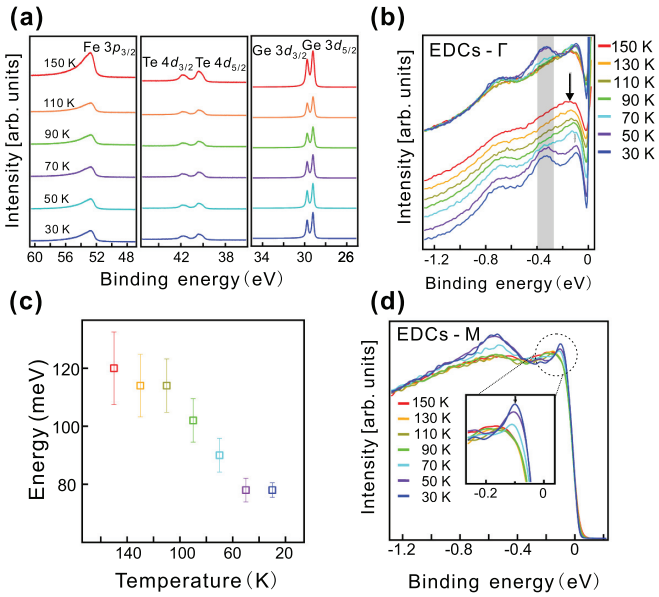

FIG. 4. Temperature dependence of the EDC peaks. (a) ARPES core level spectrum shows clear Fe $3p$, Te $4d$, and Ge $3d$ peaks with the decrease of temperature at $h\nu = 200$ eV. (b) Temperature dependence of the EDCs at Γ divided by Fermi-Dirac distribution function. (c) The energy gap defined as the peak positions indicated by the black arrow in (b) at the corresponding temperature. The thermal fluctuation is indicated by the error bars. (d) Temperature dependence of the normalized EDCs at M, and the temperature-dependent shift of the peaks indicated by the black arrow nearing the E_F is magnified.

Along the Γ-K-M direction, a continuous slow cooling process [Figs. 3(d)–3(j)] was performed carefully. A shallow electron-like band originating from the $\sqrt{3}a \times \sqrt{3}a$ $R30^\circ$ charge order is observed (the band γ^* marked by red arrow), which is discussed in detail in Fig. 5. This shallow band γ^* exists above T_{c1} and gradually fades with the decrease of temperature below T_{c1}. The temperature-dependent momentum distribution curves (MDCs) of the band β are extracted along the Γ-K-M direction at binding energy −200 meV, as shown in Fig. 3(k). The peak width of the MDCs starts to decrease when cooling below T_{c1}, and the MDC width is proportional to the inverse of the mean free path of quasiparticle (QP) scattering in ARPES measurements.

For an itinerant magnetic system, there is normally a shift of the band with the change of the magnetization. The temperature-dependent core level spectra [Fig. 4(a)] obviously exhibit Fe $3p_{3/2}$, Te $4d_{3/2}$, Te $4d_{5/2}$, Ge $3d_{3/2}$, and Ge $3d_{3/2}$ core level peaks, in which no peak shift is distinguished, and the sharp characteristic peaks confirm the chemical composition of the $Fe_{5-x}GeTe_2$ compound. This rules out the possibility that the transition point T_{c1} derives from the change of chemical valence in Fe atoms. While the neutron power diffraction measurement reported slight change of lattice parameters less than 0.1% at T_{c1} [21], the electronic structure changes near E_F are unlikely from crystal structural origin.

To characterize how the location of bands evolves with the decrease of temperature, we show the detailed temperature-dependent energy distribution curves (EDCs) taken at the Brillouin zone (BZ) center Γ [Fig. 4(b)]. Upon cooling, the spectral weight at about −400 meV binding energy [indicated by the gray shaded area in Fig. 4(b)] increases rapidly about T_{c1}, and down to low temperature (see Supplemental Material [40], Fig. s5, for the EDCs at different temperature). At the same time, the peak at −120 meV sharpens and continuously moves toward E_F with the decrease of temperature. In contrast to the position indicated by black arrow in Fig. 4(b) at $T =$ 150 K, the extracted energy position reduced from 120 meV to 78 meV relative to E_F [Fig. 4(c)]. It is recognized as a charge order induced gap feature shown in Fig. 3.

The temperature evolution of EDCs at the point M shows that a small electron pocket shifts down below the E_F around T_{c1} [indicated by the back arrow in Fig. 4(d)]. The band structure calculations reveal that the hole-like bands around Γ and electron-like bands around M are all spin-polarized (see Fig. s3 in the Supplemental Material [40]). The electron-like band at M is consistent with the itinerant ferromagnetism characteristic. It is also supported by the calculated spin-polarized density of states on Fe atoms shown in Fig. s6 in the Supplemental Material [40]. The downward movement of the electron-like band at M, thus the formation of an electron-like pocket, can cause the carrier sign change and Lifshitz transition when cooling below T_{c1}.

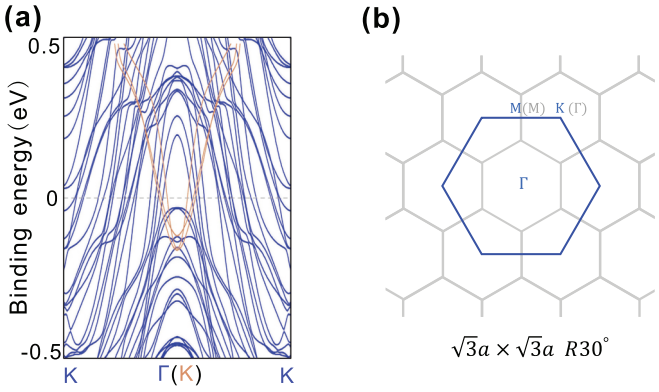

FIG. 5. Band folding along the K-Γ-K in $Fe_{5-x}GeTe_2$ and the reconstruction of Brillouin zone. (a) The band dispersion obtained from DFT calculation along the high-symmetry line K-Γ-K with the moments $M \parallel c$, and the band along the Γ-K from the charge order are superimposed, indicated by the orange lines. (b) The blue and gray hexagons represent the BZ of the primitive cell and superlattice of $\sqrt{3}a \times \sqrt{3}a$ $R30^\circ$ periodicity, respectively.

III. DISCUSSION

In this paper, the STM measurement confirmed the $\sqrt{3}a \times \sqrt{3}a$ $R30^\circ$ periodic modulation charge order in real space and the ARPES measurement detected its impact on electronic structures in reciprocal space. From the $M(T)$ curves in Fig. 1(e), the periodic modulation forms at T_{c2}, where the magnetization encounters a sudden drop in weak external magnetic fields ($B = 0.01$ T and $B = 0.1$ T). Relatively strong external magnetic field ($B = 1$ T) could suppress this periodic modulation.

A $\sqrt{3}a \times \sqrt{3}a$ $R30^\circ$ periodic modulation can lead to the reconstruction of the BZ. The corresponding reciprocal space of the superlattice is imposed on the primitive BZ [Fig. 5(b)].

The K point in the superlattice BZ coincides with Γ in the primitive BZ, and the electron-like band dispersion at K is folded back to Γ, which is obviously detected, shown as γ^* in Figs. 3(b)–3(j). Furthermore, the folded electron-like band gradually vanishes when the temperature decreases especially through T_{c1}, which indicates the $\sqrt{3}a \times \sqrt{3}a\, R30^\circ$ charge order has been suppressed. The presence of the periodic modulation will result in the rotational symmetry breaking from C_6 to C_3, and it partially restores to C_6 rotational symmetry when cooling to $T = 30$ K. Comparing the FS at $T = 150$ K and 30 K, the FS evolves from a three-petal to a hexagonal shape. This is another direct observation that the charge order is suppressed.

The change of the ferromagnetism when the temperature drops to T_{c1} needs to be discussed. The magnetic anisotropy properties in the Fe_nGeTe_2 family ferromagnets are manifested by the low temperature. An approximate temperature transition at $T \approx 110$ K has been reported in Fe_4GeTe_2, in which the easy-plane anisotropy reorients to the easy-axis anisotropy when cooling through the critical temperature driven by the small effective uniaxial magnetic anisotropy [41]. Moreover, it is reported that the Fe at the different locations in $Fe_{5-x}GeTe_2$ becomes an FM order at different temperatures [17]. Previous studies show a first-order magnetostructural transition due to the FM order of Fe(1) below T_{c1} by Mössbauer spectral and neutron diffraction [21]. A cobalt substation experiment on the composition $Fe_{5-y}Co_yGeTe_2$ at $y = 0.2$ shows that the transition at T_{c1} in $M(T)$ and $R(T)$ curves disappears [22]. It implies that Fe(1) atoms play an important role in the transition at T_{c1}. Besides, the corresponding DFT calculation shows that the dopants preferentially occupy the Fe(1) sites at $y = 0.2$ [20]. Despite the ambiguity of the mechanism happening at T_{c1}, they both show the enhancement of the ferromagnetic order when cooling through T_{c1}. The enhancement of FM suppresses the charge order below T_{c1}. It causes the C_6 rotational symmetry recovery of the FS and the fading of the band-folding feature γ^* induced by the charge order. Previous transport studies on rare-earth element compound polycrystals and first-principles calculations on monolayer $NbSe_2$ propose that the FM state could suppress the periodic modulation of charge and restore the effects on the FS caused by the modulation [42,43].

The temperature dependence of energy gap extracted from the EDCs at Γ in Fig. 4(c) shows a 50 meV decrease, which also shows the competition mechanism between the charge order and FM. The magnetoelastic effect was previously observed around $T = 110$ K via neutron power diffraction probably caused by changes in the electronic structure [17]. The lattice parameter a increases and c decreases upon cooling through T_{c1}, which can hinder the trimerization of Fe(1) atoms and weaken the charge order. In addition, the inverse mobility can be calculated by the formula $\mu^{-1} = m^* v_F / e\tau v_F = \hbar k_F \Delta k / e$, where Δk is the MDC width [44]. The abrupt decrease of resistivity at T_{c1} can be partially explained by the sudden decrease of QP scattering caused by the enhanced magnetic order at Fe(1) [21] and the suppression of charge order.

For a FM metal, the electronic bands split below Curie temperature with long-range order. The spectral weight transfer in the FM state in $Fe_{3-x}GeTe_2$ and the sensitive response of the anomalous Hall effect to the magnetic transition have demonstrated that the itinerant ferromagnetic mechanism is involved in the evolution of the electronic structure among the Fe-Ge-Te family [8,41]. With the decrease of temperature and the enhancement of the ferromagnetic order, the spin-exchange splitting between the spin-polarized bands increases. The relatively flat spin-polarized electron-like band δ at the M point shifts down below E_F when cooling through T_{c1} [Fig. 4(d)], which can explain the origins of the sign change of the Hall coefficient and the sharp decrease of the Seebeck coefficient [17,18].

In this material, the charge order and the itinerate ferromagnetism are competing for the electron density near E_F and drive the successive transitions at T_{c2} and T_{c1}. The charge order can open a gap to reduce the density of electron states at E_F. As for the itinerant ferromagnetism, there is a positive correlation between the susceptibility and the density of states at E_F. In the Stoner model, $\chi = \mu_B^2 N(E_F)/[1 - UN(E_F)/2]$, $N(E_F)$ and U are the density of states at Fermi level and the electron interaction between the spin-up and spin-down, respectively. Here we establish a unified image to depict the magnetization curves, STM, and ARPES experiments.

IV. CONCLUSIONS

In summary, we perform ARPES, STM, magnetization measurements, and the first-principles calculation to elaborate the behaviors at two critical temperatures T_{c1} and T_{c2} in the vdW ferromagnetic material $Fe_{5-x}GeTe_2$. The temperature plays a significant role in driving the competitive evolution between the charge order and the itinerant ferromagnetism, in which the electronic band structure evolution is coupled to the charge order and itinerant ferromagnetic by band folding and spin-exchange splitting. The complex magnetic transport properties in $Fe_{5-x}GeTe_2$ are also attributed to the disorder influenced by the heat treatment history of the sample, which confirms the relatively weak thermal stability in the vdW-type Fe_nGeTe_2 compounds [41]. In this work, we provide direct observation of the temperature-driven competition between the charge order and the ferromagnetism.

The relative dominance between the charge order and ferromagnetism can be controlled by either external magnetic magnitude or temperature. It is foreseeable that the equilibrium of the order states can be perturbed easily in $Fe_{5-x}GeTe_2$. As a result, resistivity, the Hall coefficient, and anisotropy induced by symmetry breaking can be tuned by broad means, such as gating, strain, and heterostructures. These rich control ways open a door to switching phenomena in spintronic devices. Theoretically, it is favorable to understand the coexistence and competition among the various orders in correlated systems like high-T_c superconductors.

ACKNOWLEDGMENTS

This work was supported by the National Natural Science Foundation of China (Grants No. 11774421, No. 11774424, No. 11774423, No. 11822412, and No. 61674045), the National Key R&D Program of China (Grants No. 2017YFA0302903, No. 2018YFE0202600, No. 2016YFA0300504, and No. 2016YFA0200700), the

Beijing Natural Science Foundation (Grant No. Z200005), the Strategic Priority Research Program (Chinese Academy of Sciences, CAS) (Grant No. XDB30000000), and the Research Funds of Renmin University of China (Grants No. 19XNLG13, No. 18XNLG14, No. 19XNLG17, and No. 21XNLG27). Computational resources were provided by the Physical Laboratory of High-Performance Computing at Renmin University of China.

[1] T. Wu, H. Mayaffre, S. Krämer, M. Horvatić, C. Berthier, W. Hardy, R. Liang, D. Bonn, and M.-H. Julien, Nat. Commun. **6**, 6438 (2015).
[2] A. J. Achkar, R. Sutarto, X. Mao, F. He, A. Frano, S. Blanco-Canosa, M. Le Tacon, G. Ghiringhelli, L. Braicovich, M. Minola, M. Moretti Sala, C. Mazzoli, R. Liang, D. A. Bonn, W. N. Hardy, B. Keimer, G. A. Sawatzky, and D. G. Hawthorn, Phys. Rev. Lett. **109**, 167001 (2012).
[3] G. Ghiringhelli, M. L. Tacon, M. Minola, S. Blanco-Canosa, C. Mazzoli, N. B. Brookes, G. M. D. Luca, A. Frano, D. G. Hawthorn, F. He, T. Loew, M. M. Sala, D. C. Peets, M. Salluzzo, E. Schierle, R. Sutarto, G. A. Sawatzky, E. Weschke, B. Keimer, and L. Braicovich, Science **337**, 821 (2012).
[4] R. M. Fernandes, A. V. Chubukov, and J. Schmalian, Nat. Phys. **10**, 97 (2014).
[5] E. P. Rosenthal, E. F. Andrade, C. J. Arguello, R. M. Fernandes, L. Y. Xing, X. C. Wang, C. Q. Jin, A. J. Millis, and A. N. Pasupathy, Nat. Phys. **10**, 225 (2014).
[6] Y. Jiang, X. Lai, K. Watanabe, T. Taniguchi, K. Haule, J. Mao, and E. Y. Andrei, Nature (London) **573**, 91 (2019).
[7] A. K. Geim and I. Grigorieva, Nature (London) **499**, 419 (2013).
[8] Y. Zhang, H. Lu, X. Zhu, S. Tan, W. Feng, Q. Liu, W. Zhang, Q. Chen, Y. Liu, X. Luo, D. Xie, L. Luo, Z. Zhang, and X. Lai, Sci. Adv. **4**, eaao6791 (2018).
[9] K. Kim, J. Seo, E. Lee, K.-T. Ko, B. S. Kim, B. G. Jang, J. M. Ok, J. Lee, Y. J. Jo, W. Kang, J. H. Shim, C. Kim, H. W. Yeom, B. I. Min, B.-J. Yang, and J. S. Kim, Nat. Mater. **17**, 794 (2018).
[10] M. A. McGuire, H. Dixit, V. R. Cooper, and B. C. Sales, Chem. Mater. **27**, 612 (2015).
[11] I. Tsubokawa, J. Phys. Soc. Jpn. **15**, 1664 (1960).
[12] M. A. McGuire, G. Clark, S. KC, W. M. Chance, G. E. Jellison, Jr., V. R. Cooper, X. Xu, and B. C. Sales, Phys. Rev. Materials **1**, 014001 (2017).
[13] B. Huang, G. Clark, E. Navarro-Moratalla, D. R. Klein, R. Cheng, K. L. Seyler, D. Zhong, E. Schmidgall, M. A. McGuire, D. H. Cobden, W. Yao, D. Xiao, P. Jarillo-Herrero, and X. Xu, Nature (London) **546**, 270 (2017).
[14] Z. Fei, B. Huang, P. Malinowski, W. Wang, T. Song, J. Sanchez, W. Yao, D. Xiao, X. Zhu, A. F. May, W. Wu, D. H. Cobden, J. H. Chu, and X. Xu, Nat. Mater. **17**, 778 (2018).
[15] Y. Deng, Y. Yu, Y. Song, J. Zhang, N. Z. Wang, Z. Sun, Y. Yi, Y. Z. Wu, S. Wu, J. Zhu *et al.*, Nature (London) **563**, 94 (2018).
[16] B. Chen, J. Yang, H. Wang, M. Imai, H. Ohta, C. Michioka, K. Yoshimura, and M. Fang, J. Phys. Soc. Jpn. **82**, 124711 (2013).
[17] A. F. May, C. A. Bridges, and M. A. McGuire, Phys. Rev. Mater. **3**, 104401 (2019).
[18] Y. Gao, Q. Yin, Q. Wang, Z. Li, J. Cai, T. Zhao, H. Lei, S. Wang, Y. Zhang, and B. Shen, Adv. Mater. **32**, 2005228 (2020).
[19] H. Zhang, R. Chen, K. Zhai, X. Chen, L. Caretta, X. Huang, R. V. Chopdekar, J. Cao, J. Sun, J. Yao, R. Birgeneau, and R. Ramesh, Phys. Rev. B **102**, 064417 (2020).
[20] C. Tian, F. Pan, S. Xu, K. Ai, T. Xia, and P. Cheng, Appl. Phys. Lett. **116**, 202402 (2020).
[21] A. F. May, D. Ovchinnikov, Q. Zheng, R. Hermann, S. Calder, B. Huang, Z. Fei, Y. Liu, X. Xu, and M. A. McGuire, ACS Nano **13**, 4436 (2019).
[22] A. F. May, M.-H. Du, V. R. Cooper, and M. A. McGuire, Phys. Rev. Mater. **4**, 074008 (2020).
[23] J. Stahl, E. Shlaen, and D. Johrendt, Z. Anorg. Allg. Chem. **644**, 1923 (2018).
[24] M. Joe, U. Yang, and C. Lee, Nano Mater. Sci. **1**, 299 (2019).
[25] S. Jiang, J. Shan, and K. F. Mak, Nat. Mater. **17**, 406 (2018).
[26] S. Jiang, L. Li, Z. Wang, K. F. Mak, and J. Shan, Nat. Nanotechnol. **13**, 549 (2018).
[27] D. MacNeill, G. M. Stiehl, M. H. D. Guimaraes, R. A. Buhrman, J. Park, and D. C. Ralph, Nat. Phys. **13**, 300 (2017).
[28] S. V. Borisenko, A. A. Kordyuk, A. N. Yaresko, V. B. Zabolotnyy, D. S. Inosov, R. Schuster, B. Büchner, R. Weber, R. Follath, L. Patthey, and H. Berger, Phys. Rev. Lett. **100**, 196402 (2008).
[29] M. D. Johannes, I. I. Mazin, and C. A. Howells, Phys. Rev. B **73**, 205102 (2006).
[30] K. Tsutsumi, Phys. Rev. B **26**, 5756 (1982).
[31] L. Bawden, S. P. Cooil, F. Mazzola, J. M. Riley, L. J. Collins-McIntyre, V. Sunko, K. W. B. Hunvik, M. Leandersson, C. M. Polley, T. Balasubramanian, T. K. Kim, M. Hoesch, J. W. Wells, G. Balakrishnan, M. S. Bahramy, and P. D. C. King, Nat. Commun. **7**, 11711 (2016).
[32] J. A. Wilson, F. J. Di Salvo, and S. Mahajan, Phys. Rev. Lett. **32**, 882 (1974).
[33] D. J. Rahn, S. Hellmann, M. Kalläne, C. Sohrt, T. K. Kim, L. Kipp, and K. Rossnagel, Phys. Rev. B **85**, 224532 (2012).
[34] E. Morosan, H. W. Zandbergen, B. Dennis, J. W. Bos, Y. Onose, T. Klimczuk, A. Ramirez, N. Ong, and R. J. Cava, Nat. Phys. **2**, 544 (2006).
[35] L. J. Li, E. C. T. O'Farrell, K. P. Loh, G. Eda, B. Özyilmaz, and A. H. C. Neto, Nature (London) **529**, 185 (2016).
[36] T. Kiss, T. Yokoya, A. A. Chainani, S. Shin, T. Hanaguri, M. Nohara, and H. Takagi, Nat. Phys. **3**, 720 (2007).
[37] F. Zwick, H. Berger, I. Vobornik, G. Margaritondo, L. Forró, C. Beeli, M. Onellion, G. Panaccione, A. Taleb-Ibrahimi, and M. Grioni, Phys. Rev. Lett. **81**, 1058 (1998).
[38] J.-J. Kim, W. Yamaguchi, T. Hasegawa, and K. Kitazawa, Phys. Rev. Lett. **73**, 2103 (1994).
[39] J. Wilson, F. D. Salvo, and S. Mahajan, Adv. Phys. **24**, 117 (1975).
[40] See Supplemental Material at http://link.aps.org/supplemental/10.1103/PhysRevB.104.165101, which includes Refs. [21,45–50], for the STM topographic image, the schematic of broken rotational symmetry, the calculated band structures and density of states, the photoemission intensity and EDC

comparison, and experimental configuration and sample description of $Fe_{5-x}GeTe_2$.

[41] J. Seo, D. Y. Kim, E. S. An, K. Kim, G.-Y. Kim, S.-Y. Hwang, D. W. Kim, B. G. Jang, H. Kim, G. Eom *et al.*, Sci. Adv. **6**, eaay8912 (2020).

[42] F. Zheng, Z. Zhou, X. Liu, and J. Feng, Phys. Rev. B **97**, 081101(R) (2018).

[43] H. Lei, K. Wang, and C. Petrovic, J. Condens. Matter Phys. **29**, 075602 (2016).

[44] T. Yoshida, S. Komiya, X. J. Zhou, K. Tanaka, A. Fujimori, Z. Hussain, Z.-X. Shen, Y. Ando, H. Eisaki, and S. Uchida, Phys. Rev. B **80**, 245113 (2009).

[45] T. T. Ly, J. Park, K. Kim, H.-B. Ahn, N. J. Lee, K. Kim, T.-E. Park, G. Duvjir, N. H. Lam, K. Jang *et al.*, Adv. Funct. Mater. **31**, 2009758 (2021).

[46] P. E. Blöchl, Phys. Rev. B **50**, 17953 (1994).

[47] G. Kresse and J. Furthmüller, Comput. Mater. Sci. **6**, 15 (1996).

[48] J. P. Perdew, K. Burke, and M. Ernzerhof, Phys. Rev. Lett. **77**, 3865 (1996).

[49] N. Marzari, A. A. Mostofi, J. R. Yates, I. Souza, and D. Vanderbilt, Rev. Mod. Phys. **84**, 1419 (2012).

[50] A. A. Mostofi, J. R. Yates, G. Pizzi, Y.-S. Lee, I. Souza, D. Vanderbilt, and N. Marzari, Comput. Phys. Commun. **185**, 2309 (2014) .